

# Dark influences III. Structural characterization of minor mergers of dwarf galaxies with dark satellites

T. K. Starkenburg<sup>1</sup>, A. Helmi<sup>1</sup>, and L. V. Sales<sup>2</sup>

<sup>1</sup> Kapteyn Astronomical Institute, University of Groningen, P.O. Box 800, 9700 AV Groningen, The Netherlands  
e-mail: tjitske@astro.rug.nl

<sup>2</sup> Department of Physics and Astronomy, University of California, Riverside, CA 92521, USA

Received date / Accepted date

## ABSTRACT

*Context.* In the current concordance cosmology small halos are expected to be completely dark and can significantly perturb low-mass galaxies during minor merger interactions. These interactions may well contribute to the diversity of the dwarf galaxy population. Dwarf galaxies in the field are often observed to have peculiarities in their structure, morphology, and kinematics as well as strong bursts of star formation without apparent cause.

*Aims.* We aim to characterize the signatures of minor mergers of dwarf galaxies with dark satellites to aid their observational identification.

*Methods.* We explore and quantify a variety of structural, morphological, and kinematic indicators of merging dwarf galaxies and their remnants using a suite of hydrodynamical simulations.

*Results.* The most sensitive indicators of mergers with dark satellites are large asymmetries in the gaseous and stellar distributions, enhanced central surface brightness and starbursts, and velocity offsets and misalignments between the cold gas and stellar components. In general merging systems span a wide range of values of the most commonly used indicators, while isolated objects tend to have more confined values. Interestingly, we find in our simulations that a significantly off-centered burst of star formation can pinpoint the location of the dark satellite. Observational systems with such characteristics are perhaps the most promising for unveiling the presence of the hitherto, missing satellites.

**Key words.** Galaxies: dwarf – Galaxies: evolution – Galaxies: interactions – Galaxies: irregular – Galaxies: starburst – (Cosmology:) dark matter

## 1. Introduction

In a Lambda cold dark matter ( $\Lambda$ CDM) universe the halo mass function is scale-free: independently of their mass, halos have their own system of substructures (van den Bosch et al. 2005; van den Bosch & Jiang 2014). Below a halo mass of  $\sim 10^{9.5} M_{\odot}$  however star formation is expected to be largely inhibited due to reionization, photo-ionization of the gas, and possibly feedback (Gnedin 2000; Hoefl et al. 2006; Kaufmann et al. 2007; Okamoto et al. 2008; Gnedin et al. 2009; Li et al. 2010; Sawala et al. 2013). The galaxy mass function is thus not scale-free, while the stellar mass-halo mass function is predicted to steepen toward lower halo masses (Behroozi et al. 2013; Moster et al. 2013; Kormendy & Freeman 2014; Garrison-Kimmel et al. 2014; Sawala et al. 2015). Therefore, dwarf galaxy halos have significantly lower baryon fractions and their satellites are expected to be predominantly completely star-less, or dark (Helmi et al. 2012).

Although the Hubble sequence (Hubble 1926) generally describes well the properties of large galaxies, on the scale of dwarfs no clear classification scheme exists. The simplest separation is given by the fact that star forming dwarfs often show irregular morphologies, while those quiescent have generally a spheroidal appearance. It is still not well understood how these classes of objects are related (see e.g. Mateo 1998; Tolstoy et al. 2009). Furthermore, blue compact dwarfs (BCDs), and more generally starbursting dwarf galaxies, have central regions that are very blue reflecting a centrally concentrated young stellar

population so bright that an underlying older, population is not readily apparent (e.g., Gil de Paz et al. 2003; Paudel et al. 2015). Just like dwarf irregulars, BCDs can furthermore depict irregular morphologies and kinematics, with star formation regions far from the center (Taylor et al. 1995; Ekta & Chengalur 2010; López-Sánchez 2010; Holwerda et al. 2013; Lelli et al. 2014; Knapen & Cisternas 2015). Off-center bursts of star formation have also been observed in a number of extremely metal-poor galaxies as well as large differences in the average line-of-sight velocities between the HI gas and the stellar component (Filho et al. 2013, 2015). As galaxy mass lowers, it appears as if a higher fraction of the systems are peculiar.

We have recently postulated that this may be partly explained by dwarf galaxies experiencing minor mergers with dark companions (Helmi et al. 2012). In Starkenburg & Helmi (2015) and Starkenburg et al. (2015), we have shown that such minor mergers can significantly alter the morphological properties of dwarf galaxies. The disturbances induced by dark objects are much more dramatic on this scale because of the lower galaxy formation efficiency (i.e. lower baryon fractions) in dwarfs compared to giant galaxies. One of the most direct imprints in gas-rich dwarfs is a vast increase in star formation: both in short bursts (during close passages of the satellite) as well as sustained high star formation rates lasting several Gyrs. In Starkenburg et al. (2015) we have shown that the general properties of our simulated dwarf systems compare very well to a large sample of

dwarf irregular galaxies and blue compact dwarfs from the literature.

In this paper we provide a quantitative characterization of the morphological and kinematic properties of the dwarf systems during the minor merger events and thereby facilitate a more detailed comparison to observations. For the analysis we use morphological descriptions that have been applied to characterize where galaxies lie along the Hubble sequence, to disentangle interacting from isolated systems, and to describe the stellar distributions in major mergers of  $\sim L_*$  or larger spiral galaxies, such as the *CAS* (Concentration, Asymmetry and Smoothness) and *GM* (Gini coefficient and M20) indicators (see e.g. Conselice et al. 2000; Conselice 2003; Abraham et al. 2003; Lotz et al. 2004, and references therein). These have also been applied to describe the stellar components of isolated irregular dwarf galaxy samples (Conselice 2003; Lotz et al. 2004), to characterise the gas distribution in starbursting dwarf galaxies (Lelli et al. 2014) and in simulations of major mergers (Holwerda et al. 2011a) as well as a variety of observational samples (Holwerda et al. 2011b,c,d,e, 2012, 2013, 2014).

This paper is organised as follows. The hydrodynamical simulations are described concisely in Sect. 2, while in Sect. 3 we focus on one specific simulated system and highlight key tidal features as the merger takes place. In Sect. 4 we introduce the morphological and kinematic indicators used and compare the results to some observational samples. We present a brief comparison to two dwarf galaxies with peculiar properties, namely IC10 and NGC6822 in Sect. 5. The summary and conclusions are given in Section 6.

## 2. Method

We analyze the structural properties of dwarf galaxies during minor mergers with dark satellites for a suite of hydrodynamical simulations recently presented in Starkeburg et al. (2015). The simulations span a range of initial conditions for the dwarf galaxy, its satellite and a variety of orbital configurations for the interaction. They were performed using the OWLS (Schaye et al. 2010) version of Gadget-3 (based on Springel et al. 2001; Springel 2005) with implementations for star formation and feedback as described in Schaye & Dalla Vecchia (2008); Dalla Vecchia & Schaye (2008).

The host dwarf galaxy consists of a dark matter halo, a stellar disk and a (generally more radially extended) gaseous disk. Both the stellar and gaseous disks follow an exponential surface density profile with radius, while the vertical distribution of the gas is determined by requiring hydrostatic equilibrium, and assuming an effective equation of state of the multiphase ISM model by Schaye & Dalla Vecchia (2008); Dalla Vecchia & Schaye (2008). Star formation occurs when the density of the gas is above a threshold of  $0.1 \text{ cm}^{-3}$ , while at lower densities the gas follows an isothermal equation of state. Feedback and stellar winds are included such that the systems, when evolved in isolation, are self-regulating over the timescale of the simulations.

The satellite is a dark subhalo (no baryons) that follows an NFW-profile with two different concentrations ( $c = 15$ ,  $c = 25$ ). In most of the simulations, it has an initial mass of 20% of that of the dwarf galaxy's halo, but we also consider 5% and 10% mass ratios. The satellite is typically placed on a fairly radial orbit with different inclinations and is launched close to its apocenter near the virial radius of the host.

For the numerical parameters, we use  $1 \times 10^6$  particles for the dwarf's dark matter halo, a softening length  $\epsilon_{\text{halo}} = 0.025 \text{ kpc}$ ,  $2 \times 10^5$  particles in baryonic mass, divided among the stellar and

gas disks according to the gas fraction  $f_g = M_{\text{gas}}/(M_{\text{gas}} + M_*)$ , with softening length  $\epsilon_{\text{bar}} = 0.008 \text{ kpc}$ . The satellite is modeled with  $1 \times 10^5$  particles that have a softening length  $\epsilon_{\text{sat}} = 0.016 \text{ kpc}$ .

We will focus mostly on one of the simulated dwarfs, which we refer to as model-A (Starkeburg et al. 2015), and which has  $M_{\text{vir}} = 5.6 \times 10^{10} M_{\odot}$ , a concentration  $c = 9$ , and  $M_* = M_{\text{gas}} = 1.4 \times 10^8 M_{\odot}$  ( $f_g = 0.5$ ). The stellar disk has a radial scale-length  $R_d = 0.93 \text{ kpc}$  and vertical scale-height  $z_0 = 0.1R_d$ . We will also report results for smaller mass systems in the range  $M_{\text{vir}} = 9.7 \times 10^9 - 2.2 \times 10^{10} M_{\odot}$ , and  $M_* = 4.4 \times 10^6 - 2.7 \times 10^7 M_{\odot}$ , with gas fractions of  $f_g = 0.75 - 0.9$ , and a range of disk thickness and halo concentrations (models B, C, and D in Starkeburg et al. 2015).

## 3. Tidal effects

As an example, we present in Fig. 1 the evolution of the model-A dwarf as it experiences a 20% minor merger. In this example the dwarf has initially a very extended gas disk, with scale length  $R_g = 4R_d$ . This set-up is motivated by observations showing that gas may spread out much farther than the stars (see e.g. Begum et al. 2008; Filho et al. 2015, and references therein).

The satellite in Figure 1 has a high concentration ( $c = 25$ ) and is launched from apocenter at a distance of  $\sim 51 \text{ kpc}$  on a fairly radial orbit with tangential velocity  $v_t = 0.5v_{\text{vir}}$ . During close passages to the disk the satellite (marked with a cross) induces large tidal tails in both the gas and stars, as shown in the second column of this figure.

During the second pericentric passage (third column of Fig. 1), the satellite meets up with a gaseous tidal tail and causes a local overdensity where star formation takes place (as can be seen from e.g. the newly born stars plotted in blue in the middle panel). The star formation rate density in this tidal structure is higher than in the center so that the brightest star forming core at this point in time is actually located more than 7 kpc from the center. Intriguingly, such features are also found in XMP galaxies (Filho et al. 2013).

Fig. 2 zooms into the gas column densities in the inner parts of the dwarf galaxy around this time. Note again the high gas densities in the tidal tails and how they correlate with the position of the satellite. Also, and as expected, the young star particles trace the motion of the satellite through the disturbed dwarf galaxy (see the blue points in the middle row of Fig. 1). Since these dominate the light, the associated local star-forming regions may well be the analogues of what is seen in XMP galaxies (Filho et al. 2013, 2015).

Figure 3 shows the star formation rate (SFR) during the encounter. The blue curve shows that the total SFR has pronounced peaks during the pericentric passages of the satellite. Interestingly, during the later passages, up to 75% ( $4 \times 10^{-3} M_{\odot} \text{ yr}^{-1}$ ) of the total star formation takes place in the tidal tail at the location of the satellite (red curve). Subsequently the total SFR increases, due to the gas that is channeled to the center, and reaches a plateau around a value that is at least a factor 10 higher than for the equivalent dwarf in isolation.

In summary, besides the characteristic starburst, signatures of the merger can be found in the morphology of the old stellar disk, the distribution and morphology of the young stellar population that is formed during the encounter, and in the morphology and kinematics of the gas. The gaseous and stellar disks show distinguishable effects both in the outskirts and in the inner parts. Interestingly, in the simulated system shown here star

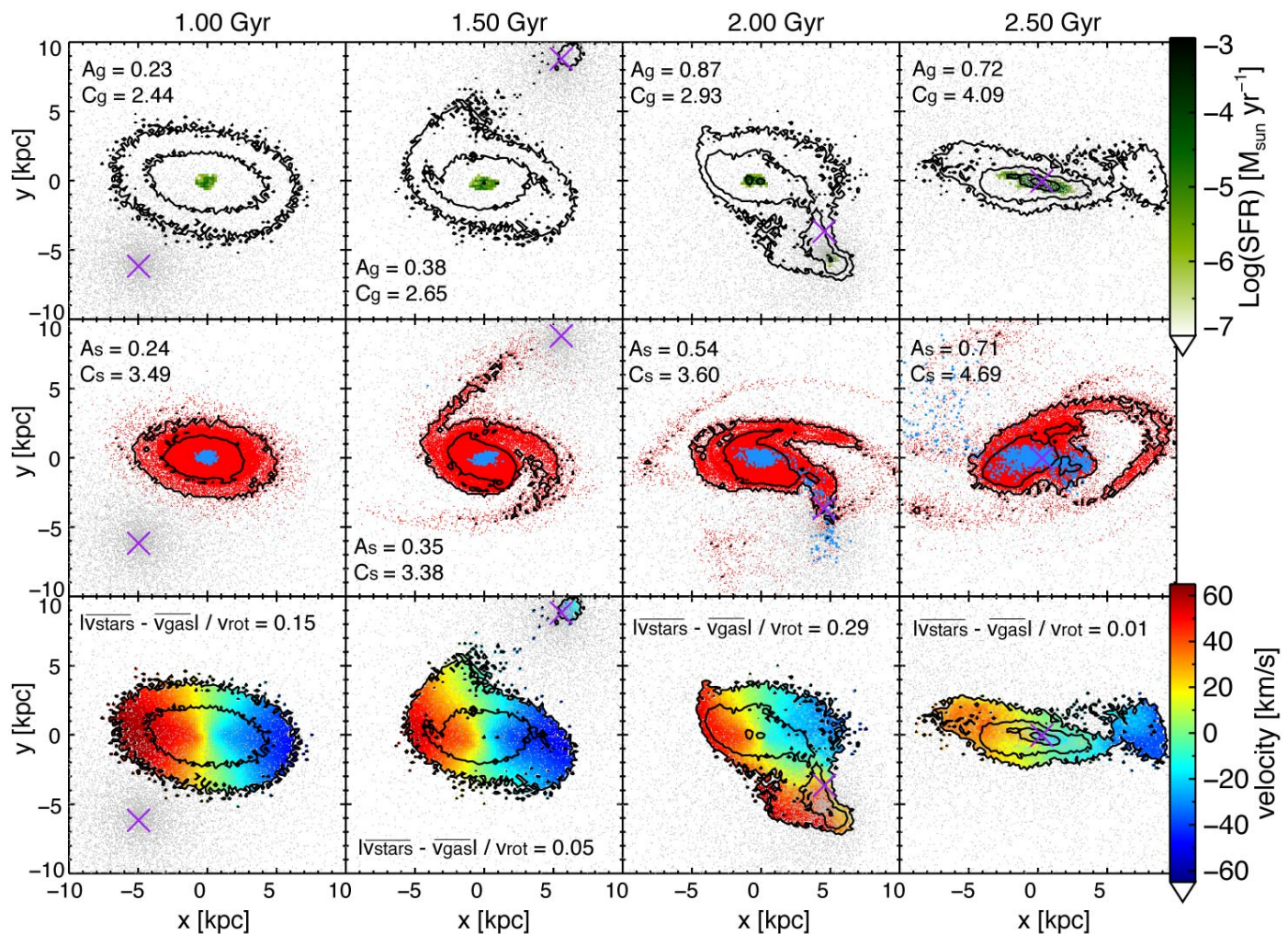


**Fig. 1.** Evolution of the model-A dwarf galaxy with  $R_g = 4R_d$ , merging with a 20% mass ratio dark satellite with  $c = 25$  on a co-planar relatively radial orbit. All figures show an inclined view of the disk, 60 deg from face-on. The top row shows the cold gas in the disk (contours at 0.4, 1, 4, and  $10 \times 10^{20} \text{ N cm}^{-2}$ ) with the star-forming gas highlighted in green (see colorbar for SFR values). The central row panels show the old stars in red, and those newly formed in blue, along with two surface brightness contours of 25 mag/arcsec<sup>2</sup> and 28 mag/arcsec<sup>2</sup>, obtained assuming an  $M/L = 0.5$  for all stellar particles. The bottom panels show the gas contours with the gas velocity maps. In all panels the satellite is shown in grey (5% of the particles are plotted), with the purple cross denoting its center of mass. The insets indicate the values of asymmetry, concentration and difference in average velocity between stars and gas computed as described in Sec. 4.

forming regions outside the center pinpoint the location of the merging dark satellite.

#### 4. Quantitative measures of structural properties

Although clear effects can be seen in the simulated dwarf galaxy which are due to the minor merger, it is important to quantify these in order to make comparisons to observations. A variety of quantitative structural descriptions of the morphology and kinematics of galaxies have been put forward in the literature. Morphologically the structure is often characterized by the CAS (concentration, asymmetry, and smoothness; Conselice 2003) and GM (Gini and M20; Lotz et al. 2004) indicators. Additionally for dwarf irregulars and BCDs, the difference in central surface brightness obtained by fitting the inner and outer regions is also used (Hunter & Elmegreen 2006; Papaderos et al. 2008). For XMP galaxies, the often used indicators include differences in the average velocity, and in the position angles of the HI gas and stellar components (Filho et al. 2015, 2013). We apply the morphological indicators to our simulations and present the re-

sults in Sect. 4.1, while we focus on the results of the kinematic indicators of the stellar and gas disks in Sect. 4.2.

##### 4.1. Morphological parameters

We estimate the morphological CAS and GM parameters, including modifications by Lelli et al. (2014); Holwerda et al. (2011d), on a grid with initial size of 20 by 20 kpc which is cropped to the regions above a fixed threshold, and a default bin size of 0.2 kpc. The thresholds adopted are close to those reported for observational studies in the literature,  $N_{\text{HI}} > 4 \times 10^{19} \text{ cm}^{-2}$  for the surface density of neutral gas and  $\mu_V < 28 \text{ mag/arcsec}^2$  for the V-band magnitude, respectively. This means that in practice each bin holds at least 12 gas particles. For the stars, assuming an average  $M/L = 0.5$ , appropriate for the V-band, each bin holds at least 4 stellar particles. The calculations are done on the stellar densities though (in  $M_\odot/\text{kpc}^2$ ).

For many of the indicators it is necessary to define the center of the system. This is done by fitting a 2-dimensional Gaussian to the projected density (although our results are robust

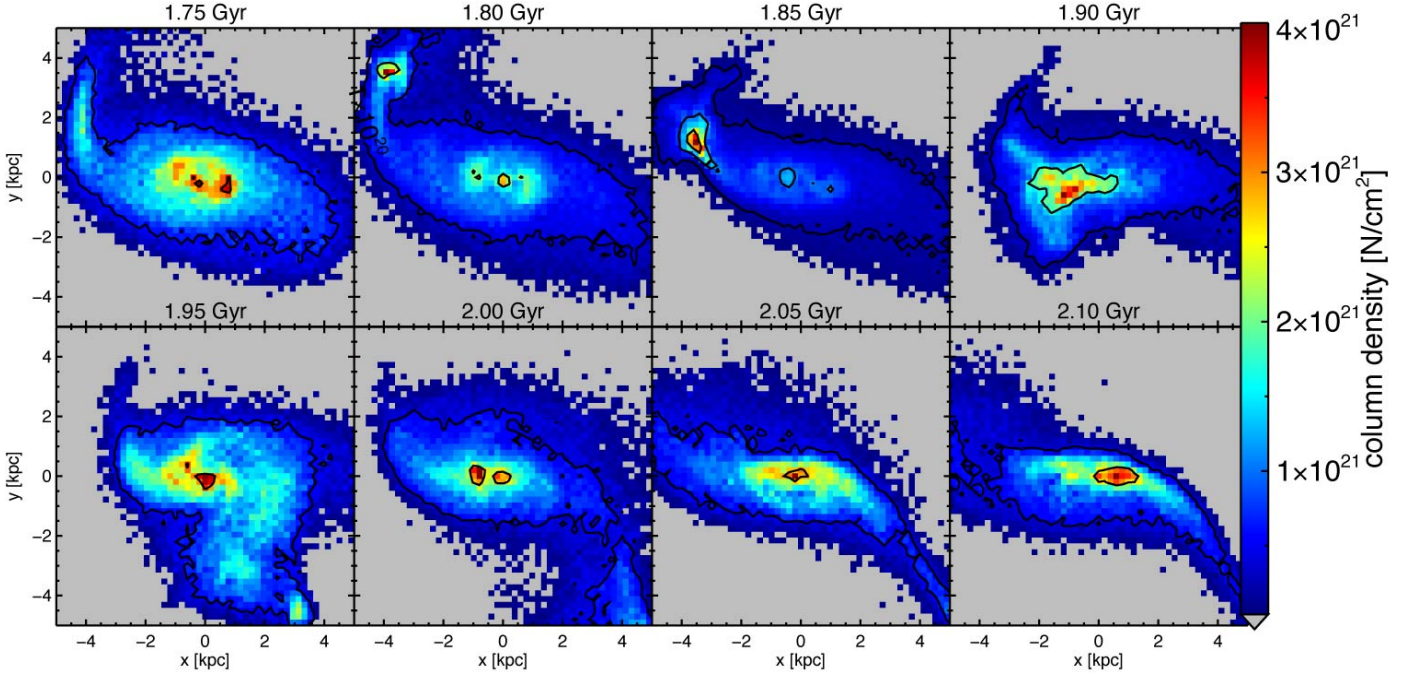


**Fig. 2.** Evolution of the inner parts of the dwarf galaxy shown in Fig. 1 around the time the satellite merges with the host. The threshold is  $0.4 \times 10^{20} \text{ N cm}^{-2}$  and the contours indicate  $1, 4, \text{ and } 10 \times 10^{20} \text{ N cm}^{-2}$ ; see colorbar for the relative values.

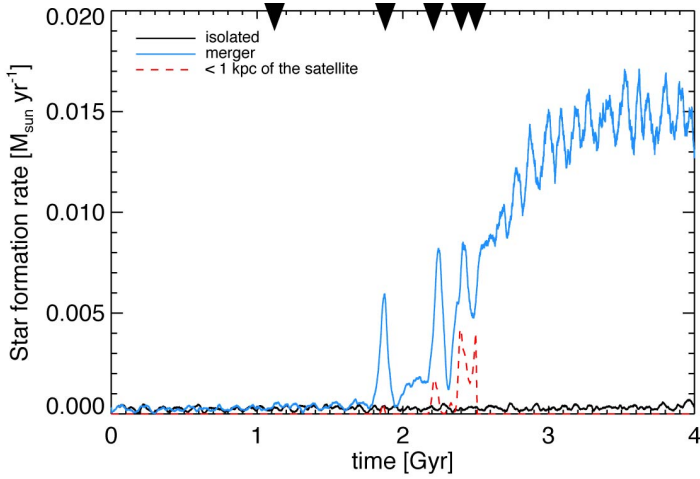


**Fig. 3.** The blue curve shows the evolution of the star formation rate of the dwarf galaxy shown in Figures 1 and 2, while the black curve is for the same model-A dwarf run in isolation. The star formation rate in the tidal tail within 1 kpc of the position of the satellite is shown with the red dashed curve, and makes up to 75% of the total SFR in the system around the time of the merger. The satellite is completely disrupted after 2.5 Gyr, but its effects on the SFR are longlasting. The pericenter passages of the satellite are indicated by the black arrows.

to the centering method used), with the threshold values described above. We have tested the effect of different thresholds ( $N_{\text{HI}} > 10^{19} \text{ cm}^2$ ,  $N_{\text{HI}} > 10^{20} \text{ cm}^2$ ,  $\mu_V < 26 \text{ mag/arcsec}^2$ , and  $\mu_V < 30 \text{ mag/arcsec}^2$ ), and assumptions regarding the mass-to-light ratios for the newly formed and original stellar populations, and found that when a sufficient area of the system is visible (as smaller systems can mostly disappear below the thresholds) the numerical values for the morphological parameters can change but the trends stay intact.

#### 4.1.1. Definitions

We now describe in detail the different morphological indicators we use in our analysis.

##### – Concentration

This describes the distribution of light over the image:

$$C = 5 \log (r_{80}/r_{20}) \quad (1)$$

where  $r_{80}$  and  $r_{20}$  are the radii which contain 80% and 20% of the total light (Conselice 2003), where for a purely exponential profile  $C = 2.7$ , and for a de Vaucouleurs profile  $C = 5.2$ . Note that since the projected surface brightness and gas column densities are computed on a grid, we determine a slightly coarse value of  $C$ .

##### – Asymmetry

This describes the relative difference in intensity when the image is rotated 180 degrees:

$$A = \frac{\sum_{i,j} |I(i,j) - I_{180}(i,j)|}{\sum_{i,j} I(i,j)} \quad (2)$$

where  $I(i,j)$  is the intensity of the pixel  $(i,j)$  (Conselice 2003). Note that with this definition,  $0 < A < 2$ .

##### – Outer Asymmetry

To give more weight to the outer parts, Lelli et al. (2014) have defined an outer asymmetry parameter as:

$$OA = \frac{1}{N} \sum_{i,j} \frac{|I(i,j) - I_{180}(i,j)|}{|I(i,j) + I_{180}(i,j)|} \quad (3)$$

(Lelli et al. 2014), where we define  $N$  as the number of the pixels with  $|I(i,j) + I_{180}(i,j)| > 0$ . Note this outer asymmetry (OA) indicator is more susceptible to noise.

Both for the  $A$  and  $OA$  parameters the detectability of asymmetries in the outskirts depend greatly on the surface

brightness or column density thresholds, especially for low mass and low surface brightness galaxies.

–  $M_{20}$

This parameter is a relative second order moment of the 20% brightest pixels and was originally introduced as an alternative to the concentration parameter:

$$M_{20} = \log \left( \frac{\sum_i^k M_i}{M_{\text{tot}}} \right) \quad (4)$$

where  $\sum_i^k I_i < 0.2I_{\text{tot}}$  and  $M_i = I_i[(x_i - x_c)^2 + (y_i - y_c)^2]$  (Lotz et al. 2004). Its advantage compared to the concentration is that there is no assumption of circular symmetry and that it is more sensitive to phenomena like multiple nuclei that are thought to be common in merging, or post-merging, systems.

– *Gini coefficient*

This statistic originally used in economics to describe the distribution of wealth within a society, was adapted to galaxy morphology by Abraham et al. (2003). It correlates with concentration but does not assume circular symmetry. We use the Gini coefficient based on the second intensity moment weighted by position:

$$G(M) = \frac{1}{2\bar{M}N(N-1)} \sum_{i,j} |M_i - M_j| \quad (5)$$

where again  $M_i = I_i[(x_i - x_c)^2 + (y_i - y_c)^2]$ , and  $\bar{M}$  denotes the mean of  $M_i$  over all  $N$  pixels (Lotz et al. 2004; Holwerda et al. 2011d).  $G(M)$  is larger when the brightest pixels are farther from the center. We only consider the pixels above the threshold in this calculation, which tends to lower the values of  $G(M)$  compared to including the background pixels.

– *Excess central surface brightness:  $|\mu_{0,HSB} - \mu_{0,LSB}|$*

We compute this by taking the difference in the central bin’s surface brightness obtained from exponential fits to the inner and outer parts of the system.

#### 4.1.2. Results

Fig. 4 shows the evolution of three morphological indicators: asymmetry, concentration and  $M_{20}$ , for the gas distributions in the system shown in Fig. 1, for five different random inclinations. This figure evidences that the indicators have a strong time dependence as the merger occurs, and that each evolves quite differently with time. For example, the asymmetry (in red) increases with time reaching a peak value when the satellite fully merges, as a consequence of the extended tidal tails clearly seen in Fig. 1, and decreases strongly afterwards. The concentration (in blue) also increases significantly around the time of the merger but it remains high afterwards, as a result of the strong central influx of gas. On the other hand, the  $M_{20}$  (in green) depicts an oscillatory behaviour with peaks that roughly coincide with each pericenter passage of the satellite. Because  $M_{20}$  is negative, and in this figure it has been normalised to the initial value, these peaks actually imply that the 20% brightest pixels are more centrally concentrated, with the dips indicating high gas densities at larger radii, suggesting that star formation occurs at larger distances. The plateau value at late times reflects the strong centrally concentrated sustained enhancement in gas

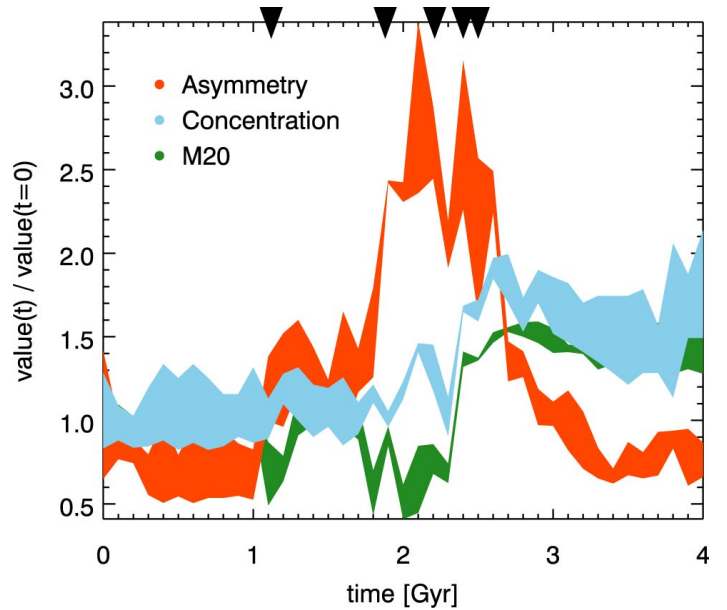


**Fig. 4.** The distribution of the asymmetry  $A$  (red), concentration  $C$  (blue), and  $M_{20}$  (green) values for the gaseous disk for 5 random inclinations in time intervals of 0.1 Gyr for the model-A dwarf during the minor merger shown in Fig. 1. These quantities have been normalised to their median (over all inclinations) initial value. The pericenter passages of the satellite are indicated by the black arrows.

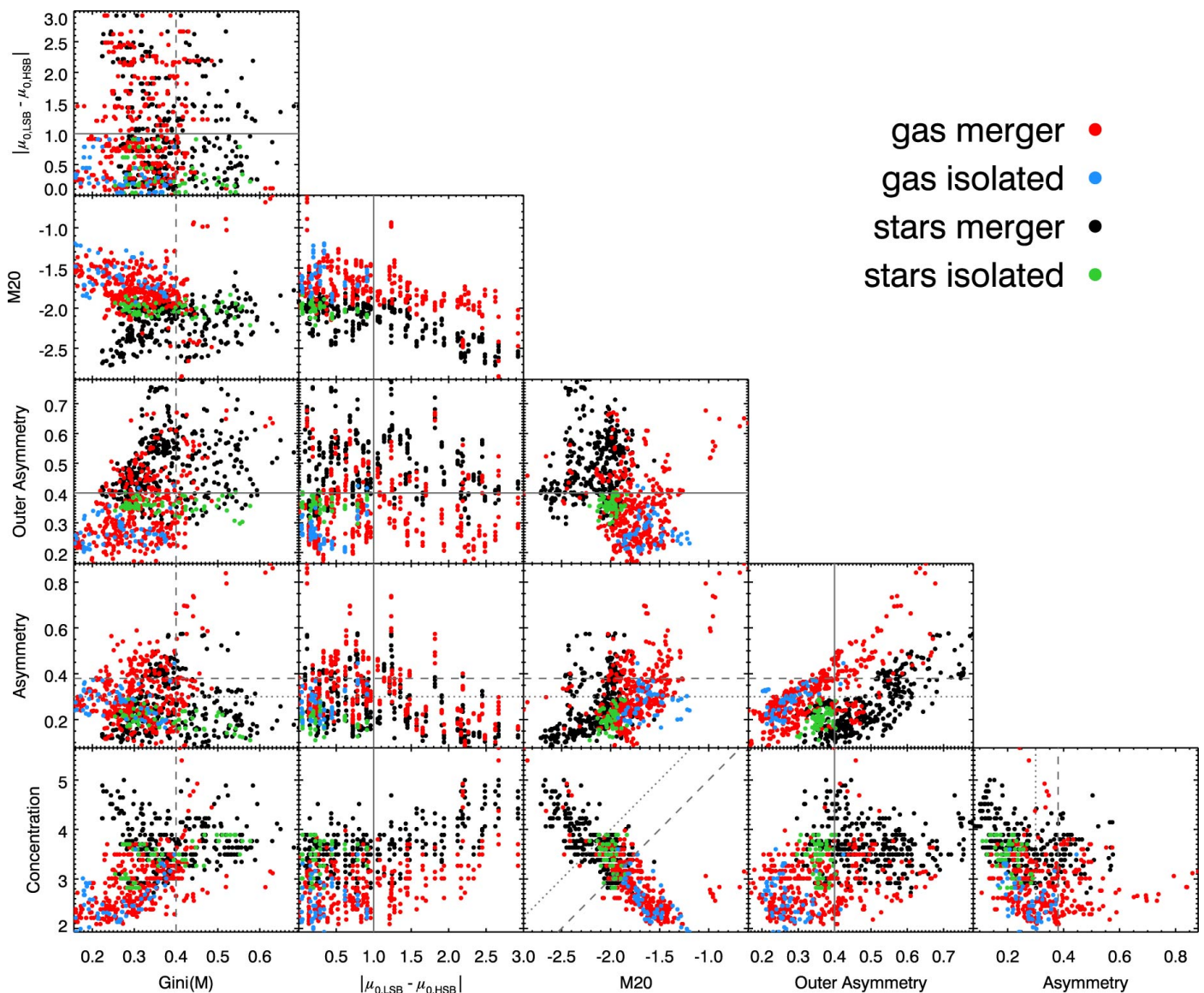
density. The parameters describing the stellar distribution follow similar trends.

Fig. 5 shows the distribution of photometric indicators for all the merger simulations we have carried out with the model-A dwarf. These simulations include a range of different orbits (orbital inclinations and eccentricities), concentrations and masses for the satellite, and varying extents of the gaseous disk. For each simulation the parameters are calculated initially (i.e. in isolation) and at 1, 2, 3, and 4 Gyr and at five random inclination angles for each point in time.

This figure shows that isolated systems (blue for gas, and green for stars) tend to occupy small regions of parameter space, whereas for mergers (red for gas and black for stars) a broad range of parameter values appears to be plausible. At face value, there is no parameter (combination) for which mergers and isolated systems can be fully separated. This might not be unexpected given the time variability of the parameters. Furthermore, cases in which the effects of the merger on the gas and stellar disks are small (e.g. if the satellite sinks in very slowly or has too low mass, or for specific viewing angles), will be hard to disentangle from systems in isolation.

Most isolated systems have low values for concentration, asymmetry, outer asymmetry, and  $G(M)$ . On the other hand, for the mergers, the asymmetry parameters for both the gas and the stars spread over a much larger range. Also the outliers in  $M_{20}$  correspond to merging systems. The difference in central surface brightness can reach up to to 3 magnitudes/arcsec<sup>2</sup> for merging systems, but is smaller than 1 magnitude/arcsec<sup>2</sup> for all isolated cases.

It is therefore easier to demark regions populated by isolated systems in the parameter subspaces plotted in Fig. 5. For example  $A < 0.38$  for the gas,  $A < 0.3$  for the stars,  $OA < 0.4$  for gas and stars,  $G(M) < 0.4$  for the gas, and a relation  $C \lesssim 2M_{20} + 7$  for the gas and  $C \lesssim 2M_{20} + 8$  for the stars. These regions are indicated by grey lines in the figure. Interestingly we find



**Fig. 5.** The concentration  $C$ , asymmetry  $A$ , outer asymmetry  $OA$ ,  $M_{20}$ , Gini( $M$ ), and excess central surface brightness  $|\mu_{0,HSB} - \mu_{0,LSB}|$ , for the gas in merger simulations (red) and in isolation (blue), and for the stars in merger simulations (black) and in isolation (green). The simulations shown correspond to the model-A dwarf, and encompass 14 different runs with varying satellite masses, halo concentrations, orbits, and radial extend of the gas disks with respect of the stellar disks (with  $R_g = R_d, 2R_d,$  or  $4R_d$ ) as described in Sect. 2. For more details on the simulations, see Starkenburg et al. (2015). The dotted, dashed and solid lines indicate regions where the isolated and merger systems are well separated for the stars, for the gas or for both, respectively.

$G(M) > 0.4$  for the HI component of merging systems, while  $G(M) > 0.6$  has been put forward by Holwerda et al. (2011d), and  $A > 0.4$  has been used for the stellar component in major mergers (Conselice 2003).

In Fig. 5 we have focused on the model-A dwarf, a relatively massive system with  $M_\star = 1.4 \times 10^8 M_\odot$ , and demonstrated that it may be possible to disentangle partly mergers from isolated systems. However, for lower mass dwarfs, with initial  $M_\star = 4.4 - 27 \times 10^6 M_\odot$ , the morphological parameters of either isolated and merging systems strongly overlap. Although a 20% merger can cause irregular features in the gas and stellar distributions (ideally resulting in higher asymmetry and outer asymmetry values), often these features are not strong enough (given reasonable thresholds) to be clearly identified by the CAS or GM indicators as being different from irregular gas densities and patchy star formation that may happen in isolation as well.

Therefore, such morphological indicators are not useful to identify merger candidates in the case of low mass dwarfs.

#### 4.1.3. Comparison to observations

Lotz et al. (2004) have estimated the asymmetry, concentration, and  $M_{20}$  parameters for 22 systems from a sample of isolated dwarf irregular galaxies observed in the B-band by van Zee (2000, 2001). Many of these systems are brighter than those in our simulations and seem to be more clumpy. Although the range of concentrations is similar ( $2.39 < C < 4.17$ ), the values for  $M_{20}$  are higher ( $-1.79 < M_{20} < -0.70$ ) than we find for the stellar components even in isolation. This implies a smoother distribution in the simulations, and this could be the result of an initial smooth set up as well as to the absence of  $H_2$  or metal-line cooling in the simulations which could induce a patchier star formation. On the other hand, the asymmetry values are in

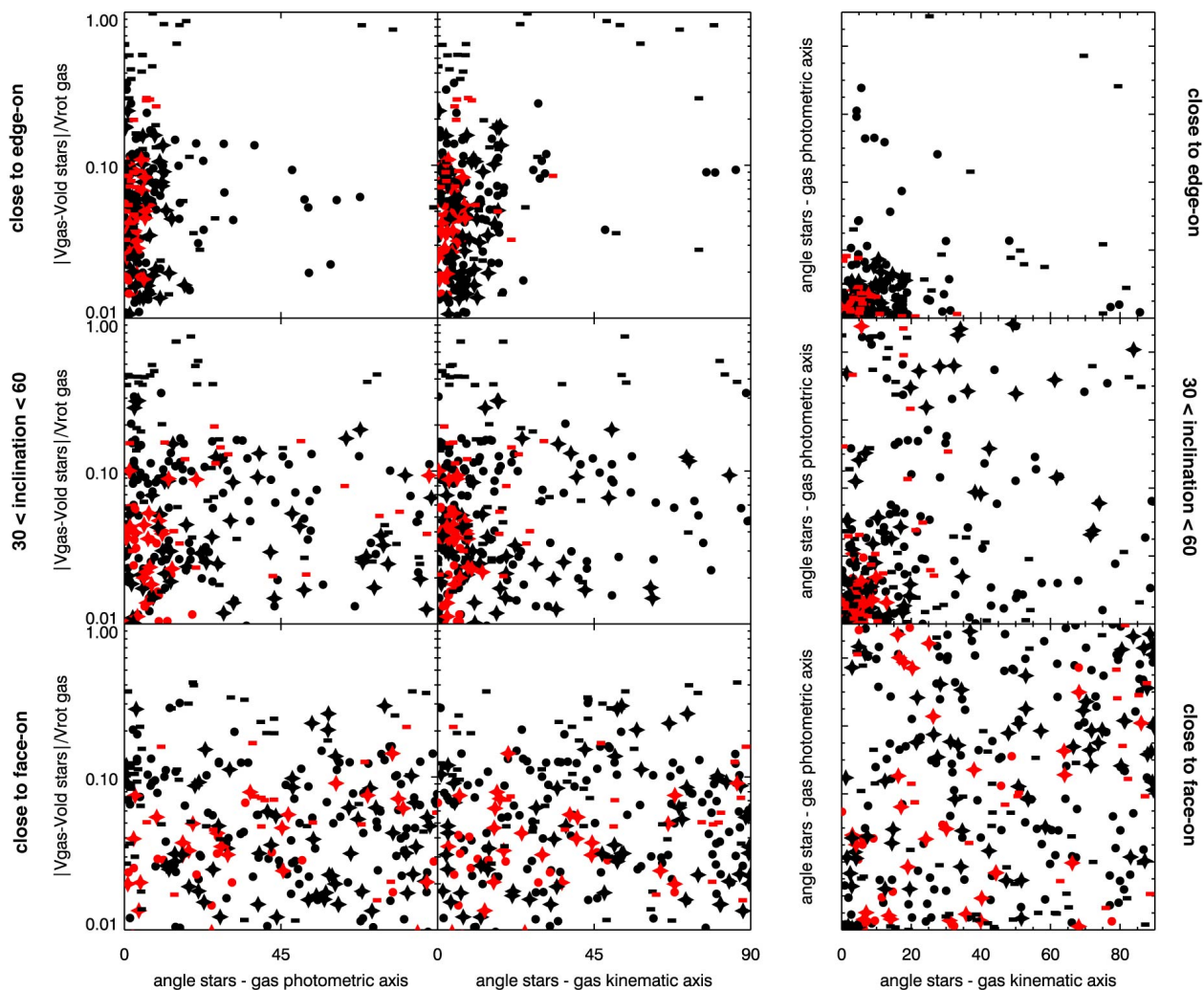


**Fig. 6.** Average velocity differences between the gas and the stellar disk normalized to the average observed rotational velocity of the gas, difference in position angle between the projected distributions of the gaseous and stellar disks, and between the projected stellar disk and the kinematic axis of the gas, for merger simulations (black) and for systems in isolation (red). The different rows correspond to different ranges of viewing angles. In this figure we have included the model-A dwarf with  $M_{\star} = 1.4 \times 10^8 M_{\odot}$  (solid circles), as well as values for systems with  $M_{\star} = 4.4 \times 10^6 M_{\odot}$  (dashes) and with  $M_{\star} = 1.1 - 2.7 \times 10^7 M_{\odot}$  (diamonds).

the range of  $0.01 < A < 0.45$  (Conselice 2003) and are consistent with what we find for the stellar components of isolated systems.

Lelli et al. (2014) have described the gas outer asymmetry for 18 starburst dwarf galaxies and for a control sample of 17 dwarf irregular galaxies from the VLA-ANGST survey (Ott et al. 2012). The outer asymmetry values of the observed starburst systems are in the range  $OA = 0.42 - 0.77$ , with a median value of  $\sim 0.6$ , i.e. similar to the values we find in our merger simulations. On the other hand, all the simulated dwarf galaxies in isolation have outer asymmetries lower than 0.4, and hence are more comparable to those in the dwarf irregular sample, which typically have  $OA \sim 0.3 - 0.5$ .

From these comparisons, we may conclude that both the stellar and gas components of dwarf irregular galaxies have similar parameter distributions to the simulated dwarfs in isolation. Furthermore, the outer asymmetries seen in the gas in observations of starburst dwarf galaxies agree with those of interacting simulated dwarfs.

#### 4.2. Kinematic parameters

Besides morphology, kinematics can also encode information about past merger events. For example, in our merger simulations the 3-dimensional direction of the total angular momentum vectors of the cold gas and of the stars can differ significantly, and up to 60 degrees, while for the isolated simulated dwarfs the difference is  $< 5$  degrees. However, angular momenta cannot be directly measured from observations and so we discuss below some of the kinematic indicators that may be used instead.

##### – Difference in average velocity between gas and stars

This has been found to be quite large for a number of extremely metal-poor (XMP) galaxies (Filho et al. 2013). In our simulations the average line-of-sight velocities are mass-weighted and computed for all particles within a bin with surface brightness or column density above the thresholds. We compare this difference to the “maximum” rotational velocity defined as  $\frac{1}{2}(|\max(v_{\text{proj}})| + |\min(v_{\text{proj}})|)$ , where these stem from the projected gas velocities within the observed region.

### – Misalignment between stars and gas

A relatively straightforward measurement consists in comparing the orientation of the major axis of the surface brightness to that of the projected cold gas distribution. These are computed by fitting a 2D-gaussian to these projected distributions.

Since measuring velocity fields for stars is challenging, in general it will not be possible to estimate the misalignment between the kinematic axes of stars and of gas. Therefore instead, we compare the orientation of the photometric major axis of the stars to the gas kinematic major axis which can easily be determined observationally from HI velocity maps.

The gas kinematic major axis is determined in our simulations using the line connecting the maximum and minimum velocities observed. To obtain an estimate of the uncertainty in the orientation we compute the kinematic axis 50 times, each time using two randomly chosen values amongst those ranked in the top 10% as maximum and minimum. From this random sampling we estimate an uncertainty of 9.8 deg, for the merging systems (lower for isolated systems). However, this estimate depends strongly on the amplitude of the velocity field, e.g. for systems close to face on, the uncertainty can be as large as  $\sim 54$  degrees.

Figure 6 presents the results for all our simulated systems. We have separated the analysis according to the projected inclination because this has a significant impact on the ability to separate isolated from merging systems.

For low mass systems (indicated by the dashes), we find the largest average velocity differences between stars and gas in mergers, while for all isolated systems, independently of their mass,  $\Delta \lesssim 0.1v_{\text{rot}}$ , and this appears to be relatively robust to inclination effects. Inspection of the simulations shows that the largest amplitude is reached around the time the satellite reaches the disk, i.e. around the first pericenter passages.

The velocity differences in our simulations are typically smaller (a few km/s) than those observed for XMP dwarfs by Filho et al. (2013)<sup>1</sup>. However, the normalised velocity differences are  $0 \lesssim \Delta_{\text{HI}}/w_{50} \lesssim 1$ , and hence consistent with those in our simulations.

Comparison of the different rows in Figure 6 directly shows that the effects of inclination are important. Especially for nearly face-on systems, the separation between mergers and isolated dwarfs is not straightforward. This is entirely due to the large uncertainties in the determination of the orientation of the photometric and kinematic axes. For example, isolated systems have close to circular spatial distributions, so that major and minor axes directions are hard to define. Furthermore, the line-of-sight velocities are typically small in this case and so also the rotation axis is not well constrained. This leads to more scatter in these distributions.

For other inclinations, the isolated systems tend to be clustered around small average velocity differences, and small misalignments. In other words, mergers are clearly more likely to have misaligned stellar photometric and gas photometric or kinematic major axes. The lack of correlation seen in the bottom left panel of Fig. 6 is a result of the misalignment between the photometric and kinematic axes for the gas in the case of mergers.

Fig. 7 provides a visual impression of a projection where the gas kinematic and the stellar distribution major axes are misaligned for the system from Fig. 1 at 2 Gyr seen for an incli-

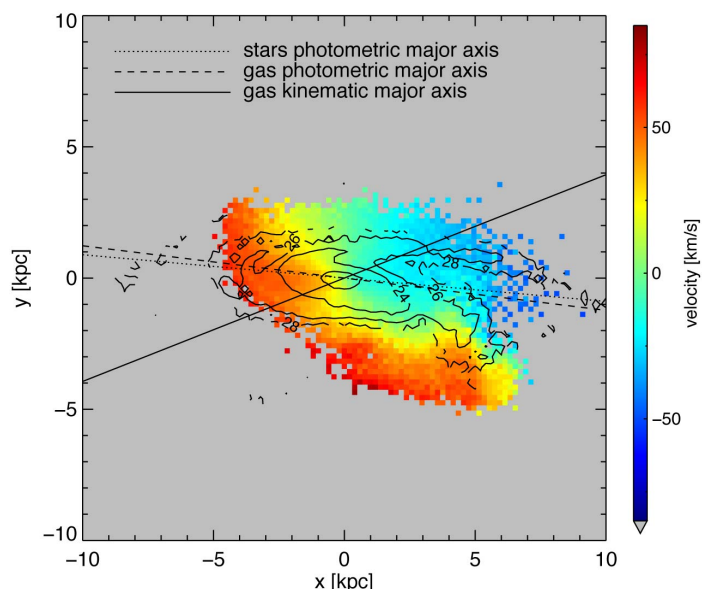


**Fig. 7.** The gas line-of-sight velocity field with the stellar surface brightness overplotted as contours for the model-A dwarf system during the minor merger shown in Fig. 1 at  $t = 2$  Gyr, but now for an inclination angle of  $i = 72.6$  deg from face-on. The kinematic axis for the gas (solid line) and the major axis of the surface brightness distribution (dotted line) are misaligned. The fitted profiles to the stellar and gas (dashed line) distributions have similar orientations, and this is because they are dominated by the behaviour in the central regions.

nation of 72.6 degrees. The gas column density distribution and stellar surface brightness distribution have roughly the same orientation (the misalignment angle is  $\sim 2$  degrees), but for both the orientation in the inner regions is different from that in the outer parts. The gas kinematic axis however has a significantly different major axis orientation, offset by  $\sim 28$  degrees.

## 5. Some intriguing cases

So far we have focused on general trends followed by our morphological and kinematic indicators, and especially on the differences between isolated and merger systems to facilitate the observational identification of dwarf galaxies undergoing a merger when the secondary is not visible, in our case being a dark satellite. We now make a rough comparison to a few intriguing cases from the literature.

The system depicted in Fig. 1 shows a distribution of gas and stars that shares characteristics with the irregular dwarf galaxy IC10: a disturbed gas and stellar distribution with multiple star forming cores and an extended HI distribution with plums and spurs with velocities that differ from that of the main gas disk (see for example Ashley et al. 2014). On the other hand, the HII regions have a low metallicity (Garnett 1990) which has been suggested as being due to the influx of fresh pristine gas from the environment (Sánchez Almeida et al. 2014). However, another interpretation is possible since as we have seen the merger leads to an extended starburst that is fueled from gas that was originally present in the outskirts of the main system, and which presumably also had a lower metallicity (see also Starkenburg et al. 2015).

Another intriguing system, though for different reasons, is the dwarf irregular galaxy NGC6822. In addition to a disturbed gas and stellar distribution and a high rate of recent star formation, this system has a star formation core located very far from

<sup>1</sup> These authors disregard offsets smaller than 10 km/s because the uncertainties and their expectation that HI velocity dispersions are  $\sim 10$  km/s for dwarf galaxies.



the center. This outer star forming region was proposed to indicate the location of a companion system, also due to a significant velocity offset (de Blok & Walter 2000), but this has been discarded because no older stellar population has been found at that location (Cannon et al. 2012). An interaction with a dark substructure will however display exactly this signature: a star formation region at a large distance without an underlying older population and a metallicity similar to the main system.

## 6. Conclusions

We have investigated the distribution of quantitative morphological and kinematic parameters (often used to characterize interacting, starburst, or peculiar systems), measured during a minor merger between a dwarf galaxy and a dark satellite. For our system with  $M_\star > 10^8 M_\odot$  the very disturbed morphologies for the gas and stellar distributions induced by the merger are reflected most notably in asymmetry parameters during the merger itself. A post-merger system however stands out the most in its high values for concentration related parameters, such as  $C$ ,  $M_{20}$  and the Gini coefficient. This is the result of an increase in central stellar and gas density due to gas being driven toward the center by tidal torques and causing a nuclear starburst episode, which can last several Gyrs.

Kinematic based parameters can be used to identify merger systems, for example via the large differences between average projected gas and stellar velocities. This works particularly well for smaller mass systems ( $M_\star < 2 \times 10^7 M_\odot$ ), for which the morphological indicators fail. Misalignments between the gas kinematic major axis and the stellar surface brightness major axis are also useful, but can only be applied for systems that are far from face-on.

Although we still have to determine the smoking-gun that will allow to determine that an interaction between a dwarf galaxy and a dark satellite has taken place, in our simulations star forming cores located far from the center actually seem to pinpoint the location of the satellite. This could be the way to shed light on a missing satellite.

*Acknowledgements.* We are grateful to Claudio Dalla Vecchia, Joop Schaye, Carlos Vera-Ciro, Alvaro Villalobos and Volker Springel for providing code. AH acknowledges financial support from the European Research Council under ERC-StG grant GALACTICA-240271 and the Netherlands Research Organisation NWO for a Vici grant.

## References

Abraham, R. G., van den Bergh, S., & Nair, P. 2003, *ApJ*, 588, 218  
 Ashley, T., Elmegreen, B. G., Johnson, M., et al. 2014, *AJ*, 148, 130  
 Begum, A., Chengalur, J. N., Karachentsev, I. D., Sharina, M. E., & Kaisin, S. S. 2008, *MNRAS*, 386, 1667  
 Behroozi, P. S., Wechsler, R. H., & Conroy, C. 2013, *ApJ*, 770, 57  
 Cannon, J. M., O’Leary, E. M., Weisz, D. R., et al. 2012, *ApJ*, 747, 122  
 Conselice, C. J. 2003, *ApJS*, 147, 1  
 Conselice, C. J., Bershad, M. A., & Jangren, A. 2000, *ApJ*, 529, 886  
 Dalla Vecchia, C. & Schaye, J. 2008, *MNRAS*, 387, 1431  
 de Blok, W. J. G. & Walter, F. 2000, *ApJ*, 537, L95  
 Ekta, B. & Chengalur, J. N. 2010, *MNRAS*, 403, 295  
 Filho, M. E., Sánchez Almeida, J., Muñoz-Tuñón, C., et al. 2015, *ApJ*, 802, 82  
 Filho, M. E., Winkel, B., Sánchez Almeida, J., et al. 2013, *A&A*, 558, A18  
 Garnett, D. R. 1990, *ApJ*, 363, 142  
 Garrison-Kimmel, S., Boylan-Kolchin, M., Bullock, J. S., & Lee, K. 2014, *MNRAS*, 438, 2578  
 Gil de Paz, A., Madore, B. F., & Pevunova, O. 2003, *ApJS*, 147, 29  
 Gnedin, N. Y. 2000, *ApJ*, 542, 535  
 Gnedin, N. Y., Tassis, K., & Kravtsov, A. V. 2009, *ApJ*, 697, 55  
 Helmi, A., Sales, L. V., Starkenburg, E., et al. 2012, *ApJ*, 758, L5  
 Hoeft, M., Yepes, G., Gottlöber, S., & Springel, V. 2006, *MNRAS*, 371, 401

Holwerda, B. W., Muñoz-Mateos, J.-C., Comerón, S., et al. 2014, *ApJ*, 781, 12  
 Holwerda, B. W., Pirzkal, N., Cox, T. J., et al. 2011a, *MNRAS*, 416, 2426  
 Holwerda, B. W., Pirzkal, N., de Blok, W. J. G., & Blyth, S.-L. 2013, *MNRAS*, 435, 1020  
 Holwerda, B. W., Pirzkal, N., de Blok, W. J. G., et al. 2011b, *MNRAS*, 416, 2437  
 Holwerda, B. W., Pirzkal, N., de Blok, W. J. G., et al. 2011c, *MNRAS*, 416, 2401  
 Holwerda, B. W., Pirzkal, N., de Blok, W. J. G., et al. 2011d, *MNRAS*, 416, 2415  
 Holwerda, B. W., Pirzkal, N., de Blok, W. J. G., & van Driel, W. 2011e, *MNRAS*, 416, 2447  
 Holwerda, B. W., Pirzkal, N., & Heiner, J. S. 2012, *MNRAS*, 427, 3159  
 Hubble, E. P. 1926, *ApJ*, 64, 321  
 Hunter, D. A. & Elmegreen, B. G. 2006, *ApJS*, 162, 49  
 Kaufmann, T., Wheeler, C., & Bullock, J. S. 2007, *MNRAS*, 382, 1187  
 Knapen, J. H. & Cisternas, M. 2015, *ApJ*, 807, L16  
 Kormendy, J. & Freeman, K. C. 2014, *ArXiv e-prints* 1407.7876  
 Lelli, F., Verheijen, M., & Fraternali, F. 2014, *MNRAS*, 445, 1694  
 Li, Y.-S., De Lucia, G., & Helmi, A. 2010, *MNRAS*, 401, 2036  
 López-Sánchez, Á. R. 2010, *A&A*, 521, A63  
 Lotz, J. M., Primack, J., & Madau, P. 2004, *AJ*, 128, 163  
 Mateo, M. L. 1998, *ARA&A*, 36, 435  
 Moster, B. P., Naab, T., & White, S. D. M. 2013, *MNRAS*, 428, 3121  
 Okamoto, T., Gao, L., & Theuns, T. 2008, *MNRAS*, 390, 920  
 Ott, J., Stilp, A. M., Warren, S. R., et al. 2012, *AJ*, 144, 123  
 Papaderos, P., Guseva, N. G., Izotov, Y. I., & Fricke, K. J. 2008, *A&A*, 491, 113  
 Paudel, S., Duc, P. A., & Ree, C. H. 2015, *AJ*, 149, 114  
 Sánchez Almeida, J., Elmegreen, B. G., Muñoz-Tuñón, C., & Elmegreen, D. M. 2014, *A&A Rev.*, 22, 71  
 Sawala, T., Frenk, C. S., Crain, R. A., et al. 2013, *MNRAS*, 431, 1366  
 Sawala, T., Frenk, C. S., Fattahi, A., et al. 2015, *MNRAS*, 448, 2941  
 Schaye, J. & Dalla Vecchia, C. 2008, *MNRAS*, 383, 1210  
 Schaye, J., Dalla Vecchia, C., Booth, C. M., et al. 2010, *MNRAS*, 402, 1536  
 Springel, V. 2005, *MNRAS*, 364, 1105  
 Springel, V., Yoshida, N., & White, S. D. M. 2001, *New A*, 6, 79  
 Starkenburg, T. K. & Helmi, A. 2015, *A&A*, 575, A59  
 Starkenburg, T. K., Helmi, A., & Sales, L. V. 2015, *ArXiv e-prints*  
 Taylor, C. L., Brinks, E., Grashuis, R. M., & Skillman, E. D. 1995, *ApJS*, 99, 427  
 Tolstoy, E., Hill, V., & Tosi, M. 2009, *ARA&A*, 47, 371  
 van den Bosch, F. C. & Jiang, F. 2014, *ArXiv e-prints* 1403.6835  
 van den Bosch, F. C., Tormen, G., & Giocoli, C. 2005, *MNRAS*, 359, 1029  
 van Zee, L. 2000, *AJ*, 119, 2757  
 van Zee, L. 2001, *AJ*, 121, 2003